Carbon dioxide reforming of methane over ordered mesoporous NiO–MgO–Al$_2$O$_3$ composite oxides

Leilei Xu [a,b], Huanling Song [a], Lingjun Chou [a,*]

[a] State Key Laboratory for Oxo Synthesis and Selective Oxidation, Lanzhou Institute of Chemical Physics, Chinese Academy of Sciences, Lanzhou 730000, PR China
[b] Graduate School of Chinese Academy of Sciences, Beijing 100049, PR China

ARTICLE INFO

ABSTRACT

Ordered mesoporous NiO–MgO–Al$_2$O$_3$ composite oxides with various Ni and Mg content were facilely synthesized *via* one pot evaporation induced self-assembly (EISA) strategy. These mesoporous materials with large specific surface areas, big pore volumes, uniform pore sizes and superior thermal stability were investigated as the catalysts for the carbon dioxide reforming of methane reaction. These materials performed high catalytic activity as well as long stability. The improved catalytic performances were suggested to be closely associated with both the amount of "accessible" active centers for the reactants owing to their advantageous structural properties and the stabilized Ni nanoparticles by mesoporous framework matrix due to the "confinement effect" of the mesopores. Besides, the role of the MgO basic modifier was also studied. It was observed that only moderate amount of the Mg containing (2 M%) could greatly promote the catalytic performances. The stabilized Ni nanoparticles as well as doped MgO had reinforced capacity of resistance to coke, accounting for no deactivation after 100 h long-term stability test at 700 °C. Therefore, the ordered mesoporous NiO–MgO–Al$_2$O$_3$ composite oxides promised a series of novel and stable catalyst candidates for carbon dioxide reforming of methane reaction.

1. Introduction

Recently, considerable attention has been paid to the catalytic carbon dioxide reforming of methane (CRM) in view of the environmental protection as well as potential industrial application aspects [1–6]. This reaction consumes two greenhouse gases simultaneously to produce valuable synthesis gas, which is the basic building block for many valuable chemicals [1,2,7]. Compared with steam reforming or partial oxidation of methane, carbon dioxide reforming of methane provides synthesis gas with a relative low H$_2$/CO ratio, which is more desirable for the direct use as feedstock for the synthesis of oxygenates, hydroformylation, oxo synthesis, and so on [8–10]. Furthermore, this reaction is usually considered as chemical energy transmission system (CETS) due to its strong endothermic characteristic, in which a power source generated from solar or nuclear energy drives this intensively endothermic reforming reaction and converts these inexpensive energies into valuable chemical energy [11–13]. Whereas, the major drawback of this catalytic process up to now remains the rapid deactivation of the catalysts originating from the sintering of the metal active sites as well as the carbon deposition [2,14,15]. Therefore, the recent

research focus and nodus in this field have been mainly concentrated on developing catalysts with favorable capacity of anti-coke and anti-sintering.

Ni based catalysts were widely investigated for the purpose due to their high initial activity and low cost. However, these catalysts are prone to suffer from quick deactivation due to the formation of the coke and thermal agglomeration of the Ni active sites, which hinder the CRM reaction from extensively industrial application [14,15]. Employment of noble metal catalysts, such as Pt, Rh Ru and Pd, can overcome these disadvantages to some degree [1,16–21]. However, considering their high cost and limited availability, it is more practical to develop stable Ni based catalysts possessing perfect anti-coke property. Various strategies aiming to improve the stability of the Ni based catalysts have been comprehensively investigated [22,23].

Former experimental and theoretical studies have confirmed that the size of the Ni particle has a significant effect on inhibiting the coke [2,3,24–28]. It is indicated that smaller Ni particles perform better ability to suppress carbon deposition. Nevertheless, confining the Ni particle size within a nano-sized range was not so straightforward because the sintering of Ni nanoparticles readily took place under the typical conditions of CRM reaction due to its low Tammann temperature [29,30]. Traditionally, minor metal particles over supported catalysts are obtained by impregnation of supports with large specific surface areas in precursors' solutions

* Corresponding author. Tel.: +86 931 4968066; fax: +86 931 4968129.
E-mail address: ljchou@licp.cas.cn (L. Chou).

[31,32]. But controlling the high dispersion of the metallic particles over the support is a tough problem because the metallic particles have intense tendency to grow up at high temperature during the process of reduction and reaction [33,34]. Taking into account the disadvantages of supported catalysts, the materials with well-defined structures, such as perovskites (La_2NiO_4) [35,36], hexaaluminates ($M_I(M_{II})_yAl_{12-y}O_{19-\delta}$, M_I = La, Sr, Ca, *etc.*, M_{II} = Ni) [37,38], spinels ($NiAl_2O_4$) [39], solid solutions (NiO–MgO) [40–43], and so on, can be used as sources of small nickel particles. Although these well-defined structures can confine the Ni particles in a nanometer range, yet their specific surface areas and pore volumes are not large enough to provide adequate "accessible" active site for the reactants.

Besides, it also has been suggested that carbon deposition can be attenuated or even suppressed as the active metal is supported on a carrier with strong Lewis basicity [44,45]. Increasing the concentration of Lewis basicity of the support enhances the chemisorption of CO_2 in the CRM reaction. Hence, the alkali metal oxides (such as K_2O, Cs_2O, *etc.*) and alkaline earth metal oxides (such as MgO, CaO, BaO) are commonly chosen as basic supports or modifiers [46–50]. On one hand, the presence of the basic modifiers promotes the process of eliminating the coke through the course that CO_2 reacts with the C to form CO, improving the stability of the catalyst. On the other hand, the chemisorption of the CO_2 activates the CO_2 molecule and augments the concentration of CO_2 on the surface of the catalyst, which is beneficial to boost the catalytic activity of the catalyst.

Guided by the above-mentioned principles, mesoporous NiO–MgO–Al_2O_3 composite oxides were designed and facilely synthesized *via* one pot evaporation induced self-assembly (EISA) strategy. The received mesoporous materials possessed excellent textural properties. In this ternary system, Ni element was dispersed uniformly among the mesoporous framework due to the special advantages of one pot synthesis method. Besides, Ni particle size was availably confined due to the "confinement effect" of the mesoporous structure. MgO acted as the basic modifier in this system and reinforced the chemisorption of CO_2 in favor of eliminating coke. The Al_2O_3 acted as the substrate and provided this material with enhanced thermal stability. Hereby, this series catalyst would simultaneously display excellent catalytic activity and stability. To the best of our knowledge, there was almost no report on ordered mesoporous NiO–MgO–Al_2O_3 materials as catalysts for CRM reaction. More details about these materials as catalysts for CRM reaction would be described specifically in the following text.

2. Experimental

2.1. Catalyst preparation

Aluminum isopropoxide ($C_9H_{21}AlO_3$, 98+%, Sigma–Aldrich), $(EO)_{20}(PO)_{70}(EO)_{20}$ triblock copolymer (Pluronic P123, typical M_n = 5800, Sigma–Aldrich), 67 wt% nitric acid (HNO_3, local vendor), nickel nitrate hexahydrate (Ni $(NO_3)_2\cdot6H_2O$, Shanghai No. 2 Reagent Factory, China), magnesium nitrate hexahydrate ($Mg(NO_3)_2\cdot6H_2O$, Beijing Shuanghuan Reagent Factory, China) and absolute ethanol (C_2H_5OH, local vendor) employed in this study were all A.R. grade. All the chemicals were used without further purification.

Mesoporous x mol% NiO–y mol% MgO–z mol% $AlO_{3/2}$ (x mol% = $n_{Ni}/(n_{Ni} + n_{Mg} + n_{Al}) \times 100\%$, $x + y + z = 100$, denoted as M-xNiyMgzAl in the following text) composite metal oxides were synthesized *via* improved one pot evaporation-induced self-assemble by fine control the volatile process based on pioneer literatures [51–53]. In a typical synthesis procedure, approximately 1.0 g $(EO)_{20}(PO)_{70}(EO)_{20}$ triblock copolymer was dissolved in 20.0 mL anhydrous ethanol with vigorous stirring. Then, 1.6 mL of 67 wt% nitric acid, approximately A mmol aluminum isopropoxide, B mmol nickel nitrate hexahydrate, C mmol magnesium nitrate hexahydrate ($A + B + C$ = 10 mmol) were sequentially added into the above solution with vigorous stirring. The final mixture was covered with PE film and stirred at room temperature for at least 5 h. Finally, transferred the mixture to a Petri dish, covered the Petri dish with holed PE film (homemade), and put the Petri dish into a 60 °C drying oven to undergo the slow EISA process for 48 h. A light green solid gel (with the increase of the Ni content, the color of the gel would deepen) was obtained after 48 h *via* precise control EISA process. The final gel was calcined by slowly increasing temperature (1 °C/min ramping rate) to 600 °C and kept at the final temperature for 5 h. As a result, the M-xNiyMgzAl composite metal oxide powders with large BET specific surface areas, big pore volumes, and narrow pore size distributions were obtained. The as-prepared mesoporous materials were pressed, crushed, and sieved through 20–40 meshes.

2.2. Catalytic activity measurements

Catalytic tests were performed at atmospheric pressure (1 atm) in a vertical fixed-bed continuous flow quartz reactor (8 mm, i.d.). The whole reaction evaluation system was consisted of a mass flow controller unit (MT50-4 J METRON Instruments), a reactor unit, and an analysis unit (SP-6800A GC). The reaction temperature increased from 650 °C to 800 °C at a 50 °C increment. The analysis for the effluent gas was carried out after stabilizing for 1 h at each studied temperature and gas hourly space velocity (GHSV). Typically, 100 mg M-xNiyMgzAl catalyst diluted with 350 mg quartz sand (20–40 meshes) was used in each run. Prior to the reaction, the catalyst was reduced in situ in a mixed flow of H_2 and N_2 (H_2:N_2 = 10:20 mL/min) with a heating rate of 1.5 °C/min to 800 °C, and maintained at 800 °C for 120 min. Before introducing in the reaction gases, the catalyst bed was purged with N_2 for half an hour to remove the absorbed hydrogen. Then, the reaction mixture was fed into the reactor *via* flow controller unit. The effluent mixed gases were cooled in an ice-water trap to remove the gaseous water generating *via* reverse water gas shift (RWGS) reaction. The separation and quantification of the products were achieved on an on-line chromatograph equipped with TDX-01 packed column.

2.3. Catalyst characterization

Powder X-ray diffraction (XRD) measurements were performed using an X'Pert Pro multipurpose diffractometer (PANalytical, Inc.) with Ni-filtered Cu Kα radiation (0.15046 nm) at room temperature from 10.0° to 80.0° (wide angle range) and 0.6° to 5.0° (small angle range). Measurements were conducted using a voltage of 40 kV, current setting of 40 mA, step size of 0.02°, and count time of 4 s. Crystallite sizes of Ni particles were calculated using Scherrer' equation: $D_{(hkl)} = K\lambda/(\beta\cos\theta)$, where K was the shape factor of the average crystalline, λ, the wavelength (1.54056 Å for Cu Kα), β, defined by a relationship between the full wave at half maximum (FWHM) of the sample and that of a quartz standard, and θ was the peak position.

The nitrogen adsorption and desorption isotherms at −196 °C were recorded on an Autosorb-iQ analyzer (Quantachrome Instruments U.S.). Prior to the tests, samples were degassed at 200 °C for 4 h. The specific surface areas were calculated *via* the BET method in the relative pressure range of 0.05–0.3; the single-point pore volume was calculated from the adsorption isotherm at a relative pressure of 0.990; pore size distributions were calculated using

adsorption branches of nitrogen adsorption–desorption isotherms by BJH method.

TEM images were taken on the JEM-2010 (Japan) high-resolution transmission electron microscopy under a working voltage of 200 kV. The samples were dispersed in absolute ethanol by moderate sonication at concentration of 5 wt% solid. A Lacy carbon-coated 200 mesh TEM micro-grid was dipped into the sample suspension and then dried under vacuum at given temperature for a while prior to analysis.

X-ray photoelectron spectroscopy (XPS) analyses of the catalysts were performed on an ESCALAB 210 (VG Scientific Ltd.) spectrometer. The fresh catalyst was placed on sample holder and pressed into self-supported wafer. An Mg target was used as the anode of the X-ray source with a power of 200 W. The pass energy of the analyzer was 30 eV in a step increment of 0.05 eV. The binding energies were calibrated using the Si (2P) line at 103.4 eV as the reference. Near-surface compositions were calculated from peak areas using the sensitivity factors, which were provided in the software of the instrument.

Thermogravimetric–different scanning calorimetry (TG–DSC) measurements were carried out on a NETZSCH STA 449F3 thermogravimetric analyzer from room temperature to 800 °C with the rate of 10 °C/min under air atmosphere.

H_2 temperature programmed reduction (TPR) measurements were performed on an AMI-100 unit (Zeton-Altamira instrument) employing hydrogen as reducing agent. The samples (250 mg) were loaded in a U-shaped quartz reactor. Prior to the TPR measurements, samples were pretreated at 300 °C for 0.5 h in flowing He (50 mL/min) to remove any moisture and other adsorbed impurities. After cooling the reactor to the room temperature, a 5% H_2–He (50 mL/min) gas mixture was introduced. The catalyst was heated to 1100 °C at a rate of 10 °C/min and the hydrogen consumption was measured using an AMETEK (LC-D-200 Dycor AMETEK) mass spectrometer.

CO_2 temperature programmed desorption (TPD) measurements were carried out on the same apparatus as described for H_2-TPR. The sample (150 mg) was pretreated at 300 °C for 2 h in a He stream (50 mL/min). After being cooled down to 20 °C, the pretreated sample was exposed in CO_2 atmosphere for 30 min. Then the sample was purged with He airstream at 20 °C until the baseline of CO_2 in the mass spectrum was steady. Finally, the CO_2-TPD was carried out with a ramp of 20 °C/min from 20 °C to the needed temperature under He stream.

Temperature programmed hydrogenation (TPH) characterizations were also operated on the same device as H_2-TPR. The spent catalyst (40 mg) was submitted to a heat treatment (10 °C/min, up to 1200 °C) in a gas flow (50 mL/min) of the mixture 5% H_2–He.

3. Results and discussion

3.1. XRD characterizations

3.1.1. XRD analysis of the as-synthesized M-xNiyMg(100 − x − y)Al materials

X-ray diffraction was one of the most important techniques for characterizing the structure of crystalline or other ordered mesoporous materials. Especially, the small angle X-ray diffraction (SXRD) had been widely used in the study of ordered mesoporous material, such as MCM-41, which was considered as the earliest reported ordered mesoporous materials, to assess the two-dimensional hexagonal structure of the sample [51–55]. As for ordered mesoporous materials, the SXRD peaks did not originate from the local order in the atomic range (also known as crystal lattice) but from the ordered channel walls of the mesoporous framework. The SXRD characterizations of M-10NiyMg(90 − y)Al
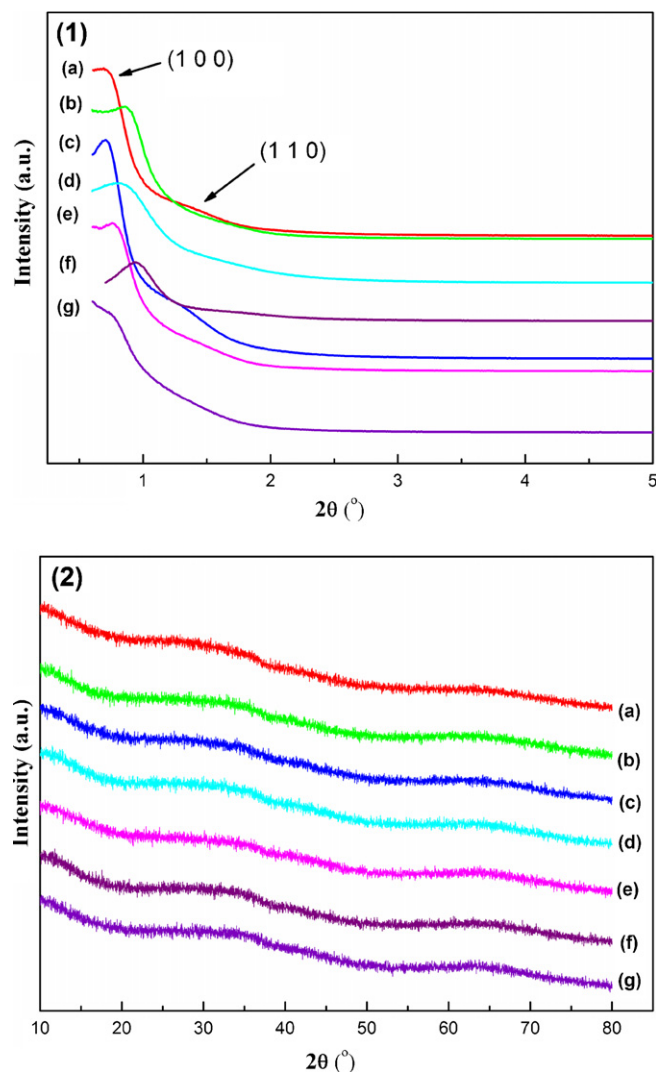

Fig. 1. Small-angle X-ray diffraction (1) and wide-angle X-ray diffraction (2) patterns of the M-10NiyMg(90 − y)Al materials calcined at 600 °C: (a) M-10Ni90Al, (b) M-10Ni1Mg89Al, (c) M-10Ni2Mg88Al, (d) M-10Ni3Mg87Al, (e) M-10Ni5Mg85Al, (f) M-10Ni8Mg82Al, (g) M-10Ni10Mg80Al.

and M-xNi2Mg(98 − x)Al materials calcined at 600 °C were performed to confirm the long-range order of the mesopores; their characterization results were displayed in Figs. 1(1) and 2(1), respectively. Almost all the M-10NiyMg(90 − y)Al clearly presented an intense (1 0 0) peak in the region of 0.8–1° and a weak (1 1 0) peak around 1.5° in Fig. 1(1), which, according to the TEM observation (see Fig. 4), could be attributed to p6mm hexagonal symmetry. As for the M-xNi2Mg(98 − x)Al with diverse Ni containing, similar to the patterns in Fig. 1(1), a strong diffraction peak (1 0 0) around 0.8° and a weak peak (1 1 0) on the vicinity of 1.5° were also detected in Fig. 2(1), suggesting that the hexagonally ordered mesopores with p6mm symmetry were also successfully obtained (refer to Fig. 4). Therefore, ordered mesoporous NiO–MgO–Al_2O_3 with various Ni and Mg molar contents were facilely prepared and the ordered mesoporous frameworks were successfully preserved after being calcined at 600 °C, demonstrating good thermal stability.

The wide angle X-ray diffraction (WXRD) patterns of the above-mentioned materials were shown in Figs. 1(2) and 2(2). Unlike the patterns of SXRD, the WXRD patterns for all the materials showed no apparent NiO, MgO and even Al_2O_3 diffraction peaks
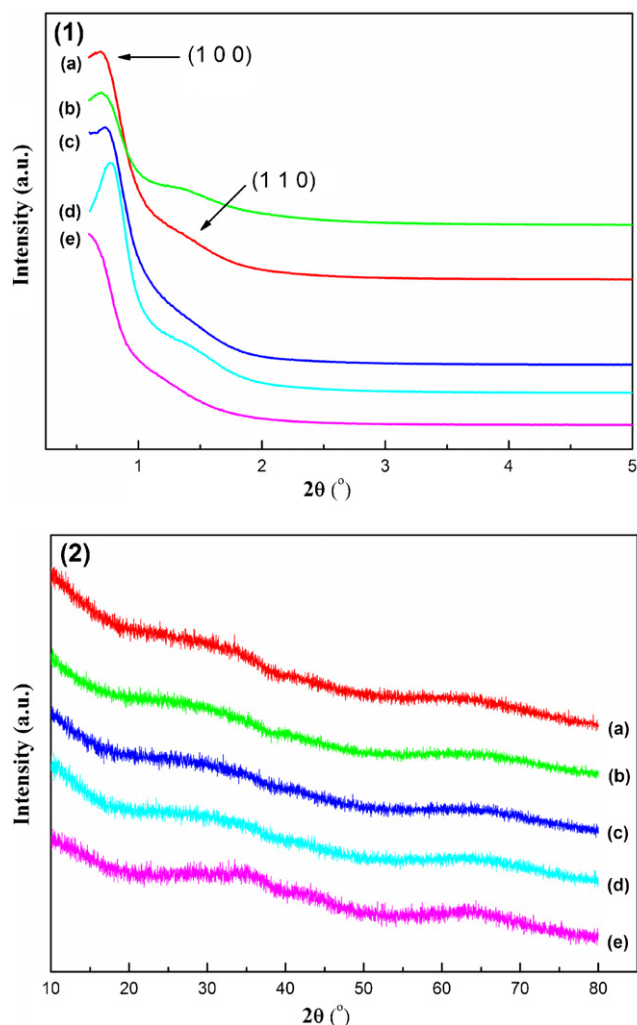
Fig. 2. Small-angle X-ray diffraction (1) and wide-angle X-ray diffraction (2) patterns of the M-xNi2Mg(98 − x)Al materials calcined at 600 °C: (a) M-1Ni2Mg97Al, (b) M-3Ni2Mg95Al, (c) M-5Ni2Mg93Al, (d) M-7Ni2Mg91Al, (e) M-15Ni2Mg83Al.

in Figs. 1(2) and 2(2), illustrating the high dispersion of NiO and MgO among the mesoporous framework of the materials. In the M-xNiyMgzAl materials, Ni and Mg atoms might be inlayed in their frameworks and segregated by the Al atoms due to the peculiar traits of this one pot preparation strategy. Therefore, the thermal agglomeration of the NiO nanoparticles during the progress of the calcination was avoided to some extent, accounting for the high dispersion of NiO particles.

3.1.2. Comparative analysis of the WXRD patterns for the as-reduced, the used, the endurance-tested M-15Ni2Mg83Al

In addition, the comparative analyses of the WXRD for the as-reduced M-15Ni2Mg83Al, the used M-15Ni2Mg83Al, and the endurance-tested M-15Ni2Mg83Al were conducted and their patterns were displayed in Fig. 3. Typically, the as-reduced catalyst was the catalyst reduced at 800 °C for 2 h in a mixed flow of H_2:N_2 (10:20 mL/min) and cooled to room temperature in the nitrogen atmosphere; the used catalyst was the catalyst tested under the conditions: CH_4/CO_2 = 1, GHSV = 15,000 mL/(g h), 1 atm, and temperature from 650 °C to 800 °C with the increment of 50 °C and stayed at each temperature stage for 70 min; the endurance-tested catalyst was the catalyst experienced 100 h lifetime stability test under given conditions: CH_4/CO_2 = 1, 700 °C,

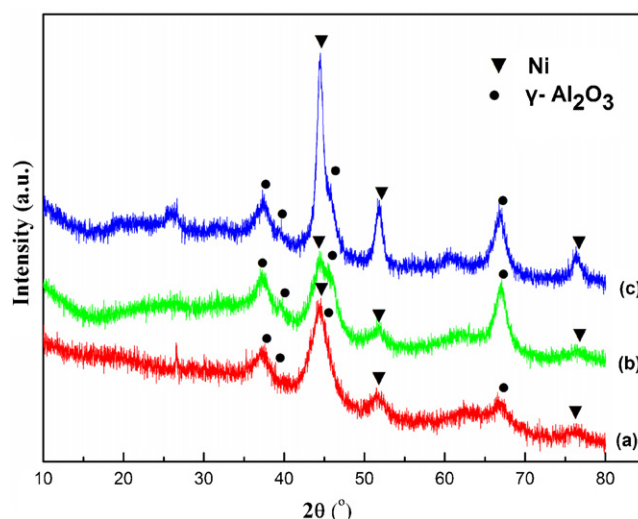**Fig. 3.** Wide-angle X-ray diffraction patterns for M-15Ni2Mg83Al catalyst after different treatments: (a) the as-reduced catalyst, (b) the used catalyst, (c) the endurance-tested catalyst.

GHSV = 15,000 mL/(g h), 1 atm. Compared with the as-synthesized M-15Ni2Mg83Al (see Fig. 2(2)), the phase transition from amorphous to γ phase for the alumina skeleton took place for the as-reduced sample because of the appearance of the diffraction peaks of γ-Al_2O_3 (JCPDS Card No. 10-0425) after being reduced at 800 °C for 2 h. Besides, the characteristic diffraction peaks of the Ni (JCPDS Card No. 87-0712) were also detected in the as-reduced M-15Ni2Mg83Al. However, it was difficult to calculate its crystallite size due to the diffraction peaks broadening, illustrating that the high dispersion state of Ni nanoparticles was maintained during the process of high temperature reduction. Compared with the as-reduced M-15Ni2Mg83Al, the used M-15Ni2Mg83Al presented a little stronger γ-Al_2O_3 diffraction intensity after undergoing different temperature stages. However, the diffraction intensities of metallic Ni in these two patterns were similar, suggesting that the sintering of the Ni nanoparticles was avoided to some degree. Compared with the aforementioned two samples, the grain size of the Ni particles of the endurance-tested M-15Ni2Mg83Al suffered slight increase. Whereas, the average $D_{(200)}$ (D was the crystallite size) of the Ni particles was only 6.60 nm calculated according to Scherrer equation and still preserved nano-sized state. The "confinement effect" of the mesoporous framework contributed to the stabilization of the metallic nanoparticles. In general, these phenomena suggested that this series of mesostructured materials possessed eminent thermal stability. In addition to this, no graphic carbon diffraction peak was observed in the patterns of the endurance-tested as well as the used samples, which was the evidence of the high anti-coke capacity of the catalyst.

3.2. Morphology analysis of as-prepared M-xNiyMgzAl

M-10N3Mgi87Al and M-7Ni2Mg91Al were selected as representatives of orderly M-xNiyMgzAl materials with various Ni and Mg contents. TEM images of these two materials calcined at 600 °C were displayed in Fig. 4. The ordered hexagonal arrangement of pores along [0 0 1] direction (Fig. 4(b)) and the alignment of cylindrical pores along [1 1 0] direction (Fig. 4(a)) for M-10Ni3Mg87Al were distinctly observed. Furthermore, the images of M-7Ni2Mg91Al (Fig. 4(c and d)) also showed similar well-ordered pore network. These TEM images further confirmed the presence of ordered mesopores
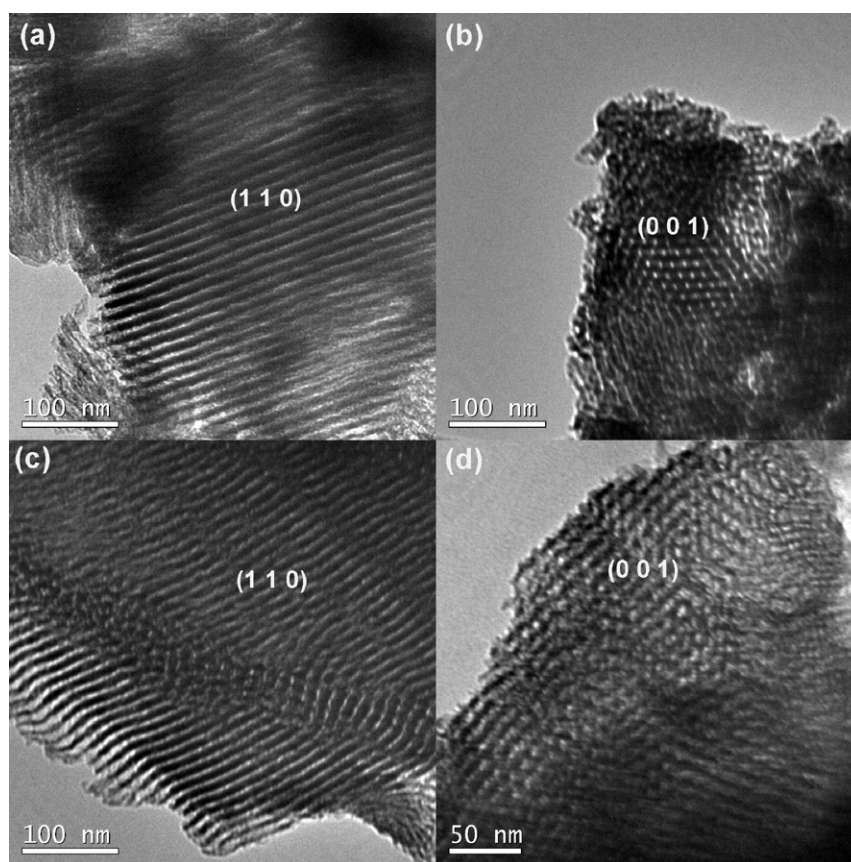
Fig. 4. TEM images of as-synthesized M-xNiyMgzAl materials calcined at 600 °C: (a) and (b) M-10Ni3Mg87Al, (c) and (d) M-7Ni2Mg91Al.

with $p6mm$ hexagonal symmetry. The characterization results of TEM were in good agreement with the SXRD characterization results.

3.3. Textural properties of the materials

3.3.1. Textural properties of the as-synthesized M-xNiyMg(100-x-y)Al materials

Similar to the XRD characterization, nitrogen physisorption could also provide the bulk information of the porous materials. The nitrogen adsorption and desorption isotherms of the M-10NiyMg(90 − y)Al and M-xNi2Mg(98 − x)Al were displayed in Figs. 5(1) and 6(1), respectively. For both batches of materials, almost all the isotherms presented in figures belonged to IV type isotherms with H1 shaped hysteresis loops, which were the significant features for ordered mesoporous materials. In addition, nearly all the capillary condensation steps of the hysteresis loops were very steep, suggesting the presence of the mesopores with excellent uniformity among the frameworks of both M-10NiyMg(90 − y)Al and M-xNi2Mg(98 − x)Al materials. The H1 shaped hysteresis loops also illuminated that all the mesopores were "cylindrical-shaped" channels, which was in good agreement with the characteristic results of SXRD and TEM images. Furthermore, the pore size distributions of these materials exhibited in Figs. 5(2) and 6(2) were all extremely narrow and the position of the peaks of the curves was all located in the range of 7–12 nm. Besides, the textural properties of the as-prepared M-xNiyMgzAl materials with varieties of Ni and Mg contents were summarized in Table 1. It could be observed that all the samples possessed large specific surface areas up to 275.130 m^2 g^{-1} and big pore volumes up to 0.614 cm^3 g^{-1}. The average pore diameters of the materials were located in the range of

7.5–12 nm without exception, belonging to "mesopore" according the definition of the IUPAC (2–50 nm).

3.3.2. Comparative analysis of the textural properties for the as-reduced, the used, the endurance-tested M-15Ni2Mg83Al

In order to investigate the thermal stability of the M-xNiyMgzAl materials, the textural properties of the as-reduced, used, and endurance-tested samples were also carefully characterized. Similar to the comparative analysis of the WXRD, the M-15Ni2Mg83Al material was also selected as an example and the characterization results were presented in Fig. 7. As for the as-reduced M-15Ni2Mg83Al, the isotherms displayed IV type isotherm with H1 shaped hysteresis loop, which indicated that the uniformity of the mesopores was still preserved after 2 h reduction at 800 °C. Furthermore, its pore size distribution was also very narrow around 8 nm. Hence, the ordered mesoporous structure of the M-15Ni2Mg83Al was successfully maintained after high temperature reduction. Whereas, the used and endurance-tested samples possessed IV typed isotherms affiliated with H2 shaped hysteresis loops. But the uniform mesopores were still maintained after 100 h lifetime endurance test according the TEM images in Fig. 17. The H2 shaped hysteresis loops might mainly derive from the blockage of the uniform mesopores by the coke, which rendered the uniform "cylindrical-shaped" mesopores deformed into "ink-bottle" shaped pores without causing the collapse of the mesoporous skeleton. But their pore size distributions were still extremely narrow around 7.50 nm. Moreover, the structural properties of these materials were also summarized in Table 1. Compared with the as-synthesized M-15Ni2Mg83Al, the as-reduced sample took on relatively smaller specific surface area and pore volume due to the shrinkage of the skeleton of the material under harsh
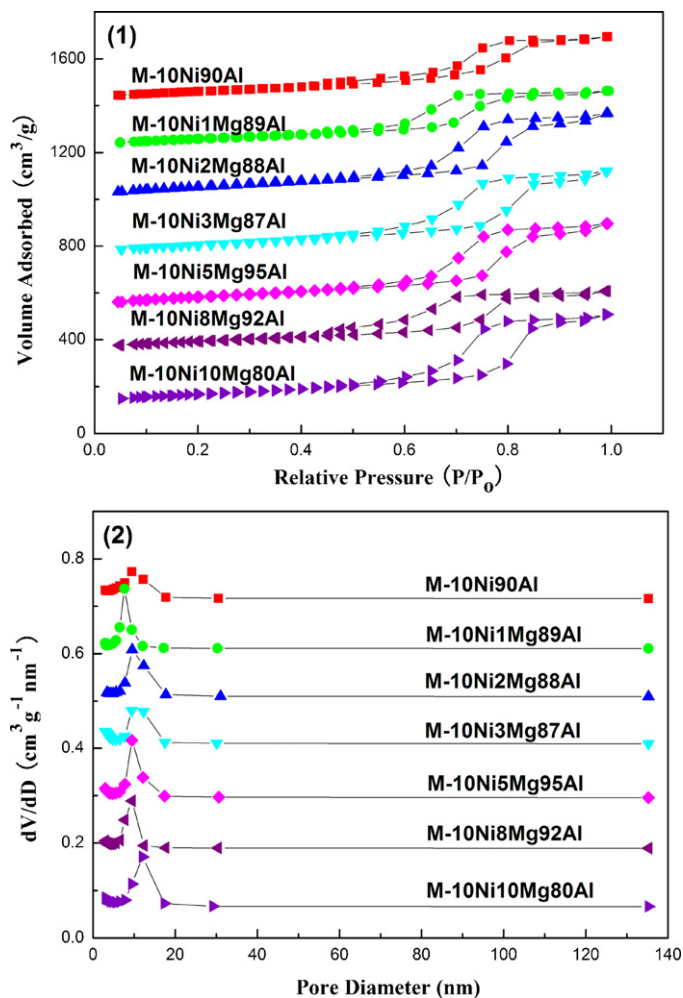
Fig. 5. Isotherms (1) and pore size distributions (2) of the M-10NiyMg(90 − y)Al materials calcined at 600 °C.
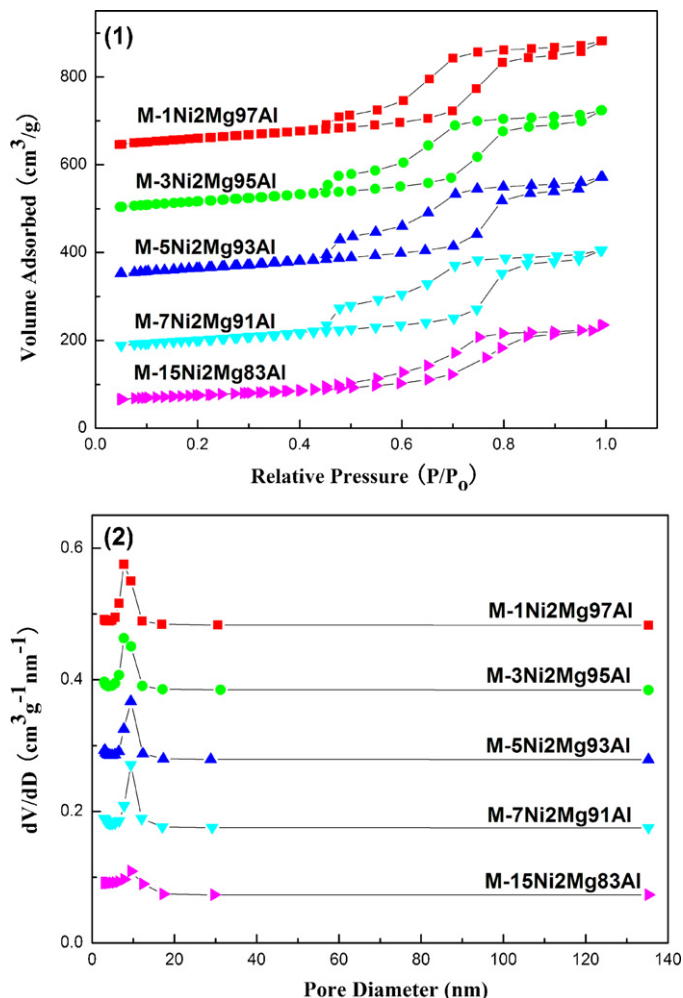

Fig. 6. Isotherms (1) and pore size distributions (2) of the M-xNi2Mg(98 − x)Al materials calcined at 600 °C.

reduction condition. Whereas, compared with the as-reduced M-15Ni2Mg83Al, the specific surface areas and pore volumes of the used and endurance-tested samples suffered further decrease. The decline in specific surface areas and pore volumes might be

caused by the carbon deposition, which blocked the mesopores to some degree. Besides, their average pore diameters were a bit smaller than that of the as-reduced one, which was originated from the further shrinkage of the mesoporous framework during the

Table 1
Textural properties of the as-prepared M-xNiyMgzAl materials calcined at 600 °C, as-reduced M-15Ni2Mg83Al, the used M-15Ni2Mg83Al, and the endurance-tested M-15Ni2Mg83Al.

Samples	Specific surface area ($m^2 g^{-1}$)	Pore volume ($cm^3 g^{-1}$)	Average pore diameter (nm)	Isotherm type
M-10Ni1Mg89Al	214.414	0.390	7.663	IV H1
M-10Ni2Mg88Al	275.130	0.596	9.543	IV H1
M-10Ni3Mg87Al	257.934	0.568	9.416	IV H1
M-10Ni5Mg85Al	273.047	0.568	9.473	IV H1
M-10Ni8Mg82Al	223.214	0.401	9.466	IV H1
M-10Ni10Mg80Al	252.859	0.614	12.074	IV H1
M-1Ni2Mg97Al	250.140	0.516	7.705	IV H1
M-3Ni2Mg95Al	233.916	0.485	7.715	IV H1
M-5Ni2Mg93Al	239.249	0.483	9.420	IV H1
M-7Ni2Mg93Al	243.419	0.476	9.415	IV H1
M-15Ni2Mg83Al	214.533	0.380	9.501	IV H2
The as-reduced M-15Ni2Mg83Al[a]	185.936	0.370	8.035	IV H1
The used M-15Ni2Mg83Al[b]	133.107	0.266	7.793	IV H2
The endurance-tested M-15Ni2Mg83Al[c]	140.718	0.292	7.820	IV H2

[a] The M-15Ni2Mg83Al catalyst was in situ reduced under H_2/N_2 (H_2:N_2 = 10:20 mL/min) atmosphere at 800 °C for 2 h.
[b] The used catalyst was the catalyst tested under the conditions: CH_4/CO_2 = 1, GHSV = 15,000 mL/(g h), 1 atm, and temperature from 650 °C to 800 °C with the increment of 50 °C and stayed at each temperature stage for 70 min.
[c] The M-15Ni2Mg83Al material was used as catalyst of CRM reaction for 100 h long-term stability test; reaction conditions: CH_4/CO_2 = 1, GHSV = 15,000 mL/(g h), 700 °C, 1 atm.
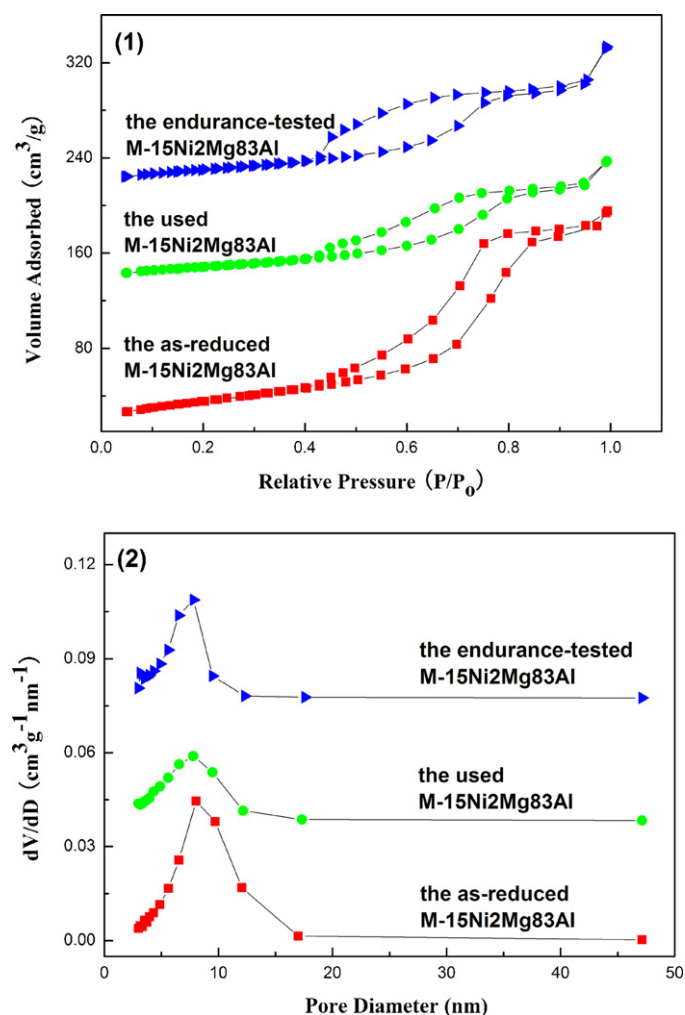
Fig. 7. Isotherms (1) and pore size distributions (2) of the M-15Ni2Mg83Al catalyst after different treatments: (a) the as-reduced catalyst, (b) the used catalyst, (c) the endurance-tested catalyst.

process of the reaction. Although the specific surface areas, pore volumes and pore diameters suffered from certain damage during the harsh reduction and reaction conditions, yet the mesostructure and narrow pore size distributions of the materials were successfully preserved. Therefore, evidences mentioned above once again demonstrated the excellent thermal stability of this series of materials.

3.4. XPS analysis

Table 2 provided the binding energies of the surface elements of the M-10NiyMg(90 − y)Al materials measured by XPS. It was found that the binding energies of the surface elements Ni, Al, Mg and O were not affected by Mg modification with various contents, that is, their valence states were unchanged basically. Therefore, the addi-

Table 2
Binding energy (eV) of the surface elements of the M-10NiyMg(90 − y)Al materials.

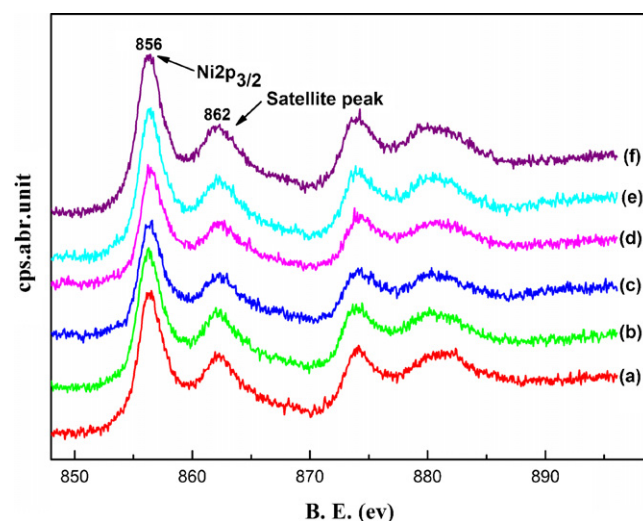| y	Mg1s	Ni2p$_{3/2}$	Al2p	O1s
0	–	856.38	74.44	531.51
1	1304.21	856.28	74.37	531.43
2	1304.22	856.39	74.49	531.60
5	1304.24	856.40	74.49	531.66
8	1304.33	856.47	74.51	531.72
10	1304.20	856.31	74.38	531.54

Fig. 8. XPS spectra of the Ni element in M-10NiyMg(90 − y)Al materials calcined at 600 °C with different Mg contents: (a) M-10Ni90Al, (b) M-10Ni1Mg89Al, (c) M-10Ni2Mg88Al, (d) M-10Ni5Mg85Al, (e) M-10Ni8Mg82Al, (f) M-10Ni10Mg80Al.

tion of MgO did not alter the electronic environment of these ions based on the consistency of their binding energies. Thus, based on the standard binding energy data, it could be concluded that their oxidation states were Ni^{2+}, Al^{3+}, Mg^{2+}, O^{2-}, respectively. Besides, from the XPS spectra (exhibited in Fig. 8) of Ni on the surface, it was observed that the locations of Ni2p$_{3/2}$ peaks for all the samples were centered around 856.4 eV and were accompanied by a shake-up satellite peak at 862.0 eV, which were the typical characteristics of nickel species for NiAl$_2$O$_4$ spinel according to the pioneer literatures [37,38,56]. Generally, the binding energy of Ni2p$_{3/2}$ in pure NiO was about 853.6 eV. Therefore, the elemental Ni in the M-10NiyMg(90 − y)Al ought to present itself in the form of NiAl$_2$O$_4$ spinel-like species instead of pure NiO.

3.5. Reducibility of the M-xNiyMgzAl catalysts

3.5.1. Reducibility of the M-10NiyMg(90 − y)Al catalysts

TPR was an effective technique for examining the reducibility of the metal oxide based catalysts. TPR profiles of M-10NiyMg(90 − y)Al samples with diverse Mg contents were shown in Fig. 9. All the samples exhibited similar profiles of hydrogen reduction, behaving only one pronounced reduction peak in the range of 660–741 °C regardless of the Mg loading. On the contrary, there was no reduction peak appearing in the region of 300–400 °C, which was assigned to the reduction of free NiO not intensively interacting with the support. Irrespective of the Mg loading, all the catalysts possessed much higher reduction temperature than the free NiO, indicating the formation of the strong interaction between Ni and the mesoporous framework, such as NiAl$_2$O$_4$ spinel-like species based on the former XPS analysis (refer to Fig. 8). It could also be observed that the reduction peak gradually shifted towards low temperature with the increase of Mg loading for almost all the catalysts. The reason for this trend might derive from the competition between nickel and magnesium for interaction with alumina. Magnesium would tend to form magnesium aluminate (MgAl$_2$O$_4$), reducing the opportunity of the subsequent formation of the nickel aluminate (NiAl$_2$O$_4$) spinel-like species. The later with higher Mg content would present weaker interaction towards alumina, resulting in the reduction of the Ni species at relatively lower temperatures [49].
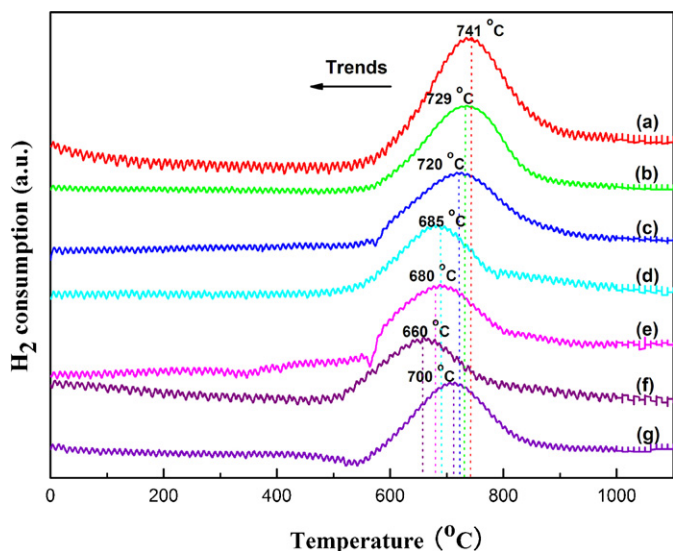
Fig. 9. TPR profiles of the M-10NiyMg(90 − y)Al materials calcined at 600 °C with different Mg contents: (a) M-10Ni90Al, (b) M-10Ni1Mg89Al, (c) M-10Ni2Mg88Al, (d) M-10Ni3Mg87Al, (e) M-10Ni5Mg85Al, (f) M-10Ni8Mg82Al, (g) M-10Ni10Mg80Al.

3.5.2. Reducibility of the M-xNi2Mg(98 − x)Al catalysts

TPR profiles of M-xNi2Mg(98 − x)Al with various Ni contents were displayed in Fig. 10. Similar to the profiles of M-10NiyMg(90 − y)Al, all the samples also took on only one
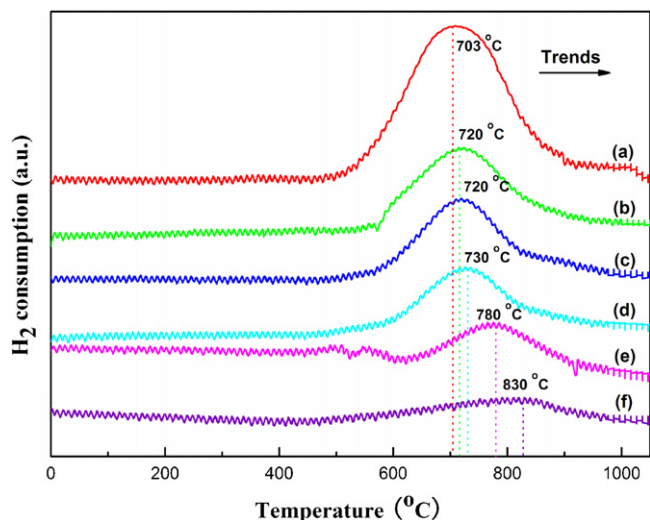

Fig. 10. TPR profiles of the M-xNi2Mg(98 − x)Al materials calcined at 600 °C with various content: (a) M-15Ni2Mg83Al, (b) M-10Ni2Mg88Al, (c) M-7Ni2Mg91Al, (d) M-5Ni2Mg93Al, (e) M-3Ni2Mg95Al, (f) M-1Ni2Mg97Al.

remarkable reduction peak in the region from 703 °C to 830 °C regardless of the Ni content. The typical feature of the reduction peak for dissociated NiO also did not emerge in the low temperature region (300–400 °C), either, suggesting that the intense interaction between the Ni species and the framework had been also established. Furthermore, with the decrease of the Ni loading from 15% to 1%, the uptake of the hydrogen consumption peak became lower due to the decrease in the Ni content. Apart from this, the reduction peak gradually migrated towards high temperature as the Ni loading decreased, which might be related to the facile formation of the $NiAl_2O_4$ spinel-like species in the case of lower Ni loading and relatively higher alumina percentage.

3.6. CO₂-TPD analysis

CO_2-TPD was performed to determine the basicity of the catalysts. Generally, it was considered that CO_2 adsorbed on weaker basic sites was desorbed at low temperature and that adsorbed on strong basic sites was desorbed at high temperature [57]. The CO_2-TPD patterns of the M-10NiyMg(90 − y)Al catalysts with different Mg contents from 0% to 10% were detailedly compared in Fig. 11(1). However, the TPD profiles for all the samples were identical in shapes. As it could be seen, all the catalysts showed a strong CO_2 desorption peak around 170 °C. Especially, it could be clearly observed that the M-10Ni90Al catalyst without any Mg promotion still possessed an intense desorption peak around 170 °C. It also could be found that with the increase of the magnesium content the intensity of the desorption peak around 170 °C was increased. Therefore, based on aforementioned phenomena, it could be speculated that this desorption peak might be derived from both the weakly chemisorbed CO_2 of the framework as well as the physically adsorbed CO_2 due to the large pore volumes and specific surface areas possessed by these catalysts. Besides, another three desorption peaks centered around 655 °C, 799 °C and 891 °C were also observed for all the catalysts in spite of the latter two peaks overlapping. As for the latter two overlapped desorption peaks, their strength was closely related to the addition of the Mg. However, the relationship between the intensity of the peak around 655 °C and magnesium content was very ruleless. These three peaks mentioned above might be related to the strongly chemisorbed CO_2. In order to investigate these TPD profiles meticulously, Lorentz mathematical model was used to resolve the overlapped desorption peaks. Took the M-10Ni1Mg89Al as an example, four distinct desorption peaks centered at 177 °C, 640 °C, 815 °C and 903 °C were distinctively observed in Fig. 11(2). This implied that more than one sort of basic centers with different intensities existed among the mesoporous framework of the M-10NiyMg(90 − y)Al materials including M-10Ni90Al. Overall, the categories of the basic centers for M-10NiyMg(90 − y)Al were abundant due to their own structural features as well as the promotion of the MgO.
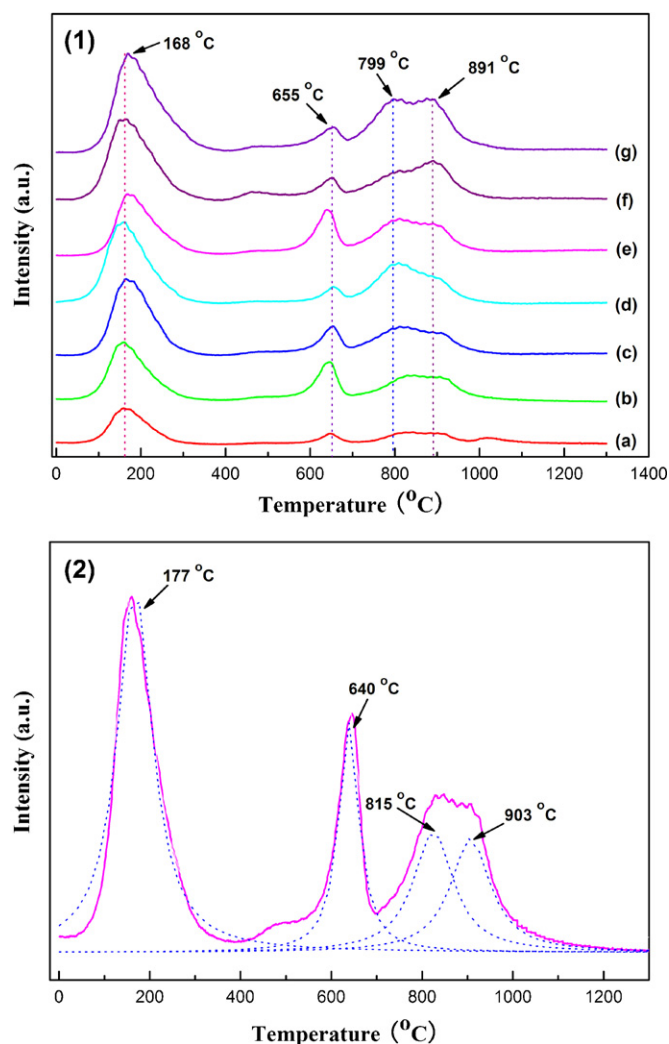
Table 3
The average conversions of the CH_4, CO_2 and H_2/CO ratios for the CRM reaction over M-10NiyMg(90 − y)Al catalysts at various temperatures; reaction conditions: CH_4/CO_2 = 1, GHSV = 15,000 mL/(g h), 1 atm.

Samples	650 °C			700 °C			750 °C			800 °C		
	C_{CH_4}	C_{CO_2}	H_2/CO	C_{CH_4}	C_{CO_2}	H_2/CO	C_{CH_4}	C_{CO_2}	H_2/CO	C_{CH_4}	C_{CO_2}	H_2/CO
M-10Ni90Al	61.54	68.40	0.8045	76.86	82.62	0.8386	87.45	90.89	0.8798	94.08	95.93	0.8838
M-10Ni1Mg89Al	61.60	68.34	0.8085	77.16	82.53	0.8380	87.75	91.27	0.8802	93.07	95.78	0.9020
M-10Ni2Mg88Al	66.08	71.45	0.8448	80.94	85.69	0.8601	90.22	93.32	0.8876	95.08	96.25	0.8859
M-10Ni3Mg87Al	62.93	70.54	0.8428	78.62	83.84	0.8596	88.81	91.40	0.8872	94.30	96.65	0.9110
M-10Ni5Mg85Al	62.51	69.61	0.8202	78.19	84.69	0.8545	88.45	92.53	0.8734	94.71	96.32	0.8951
M-10Ni8Mg82Al	62.28	69.15	0.8018	78.21	84.15	0.8573	88.19	92.52	0.8794	94.37	96.17	0.8990
M-10Ni10Mg80Al	59.75	67.27	0.8159	75.82	81.57	0.8450	85.39	91.23	0.9014	93.21	95.17	0.9021

Fig. 11. (1) CO_2-TPD profiles of the M-10NiyMg(90−y)Al materials calcined at 600 °C with different Mg contents: (a) M-10Ni90Al, (b) M-10Ni1Mg89Al, (c) M-10Ni2Mg88Al, (d) M-10Ni3Mg87Al, (e) M-10Ni5Mg85Al, (f) M-10Ni8Mg82Al, (g) M-10Ni10Mg80Al; (2) the fine structure of the CO_2-TPD profile of the M-10Ni1Mg89Al.

3.7. Catalytic performances

3.7.1. The effect of the magnesium modifier

Blank test was carried out prior to regular catalytic experiments and showed negligible catalytic activity. The initial catalytic activities of the M-10NiyMg(90−y)Al catalysts with different Mg contents under typical reaction conditions ($CH_4/CO_2 = 1$, GHSV = 15,000 mL/(g h), 1 atm) were shown in Table 3. Generally, the conversions of CH_4 and CO_2 strongly depended on reaction temperature and all the catalysts showed their respective highest catalytic activity at 800 °C due to the intensely endothermic character of the CRM reaction [2]. Besides, it could be clearly found that the conversion of the CO_2 was a bit higher than that of the CH_4 for most of the temperature stages investigated because of the concomitance of the reverse water–gas shift reaction. By the same token, the H_2/CO ratios were always less than the stoichiometric ratio (~1) for CRM reaction. However, the H_2/CO ratios were elevated as the reaction temperature increased, because the RWGS reaction would gradually be suppressed with the increase of reaction temperature and completely be inhibited at around 820 °C based on thermodynamic analysis. Furthermore, CH_4, CO_2 conversions of these M-10NiyMg(90−y)Al catalysts were all close to or
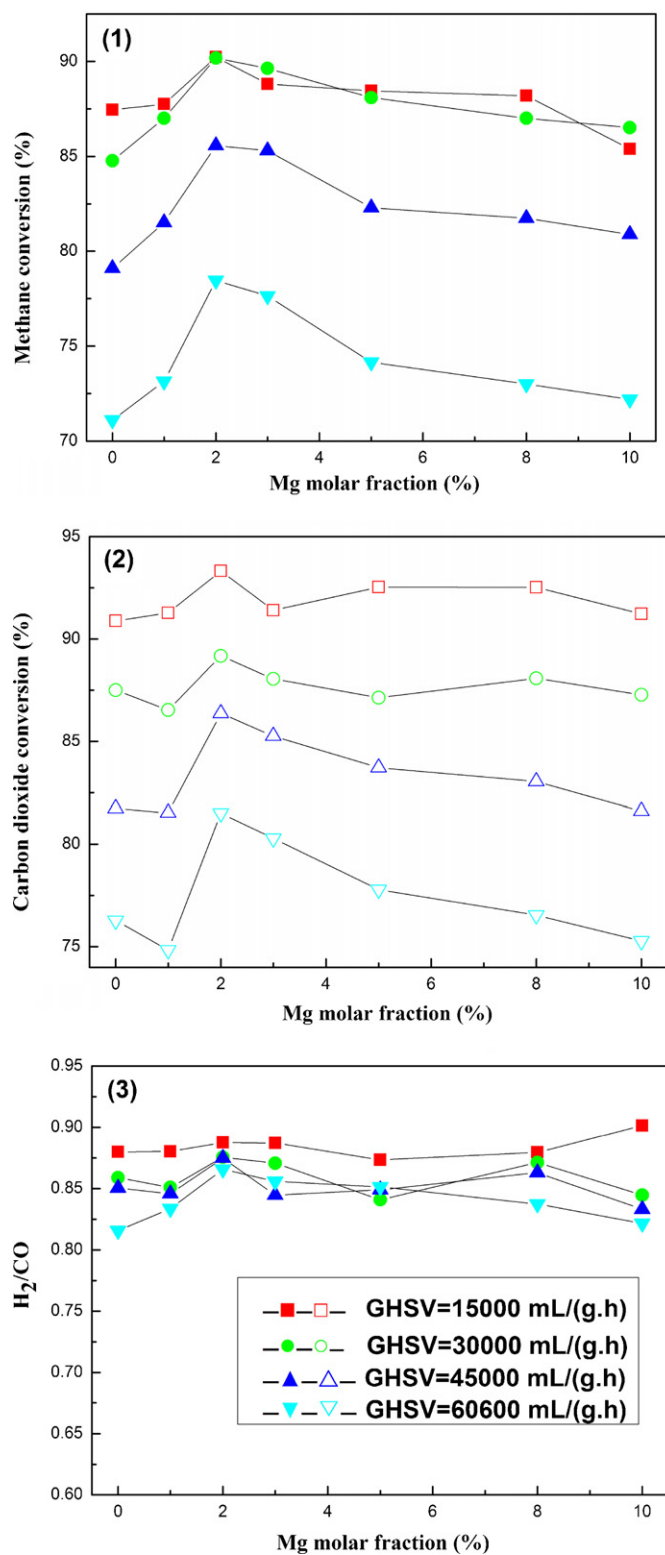

Fig. 12. The curves of the (1) CH_4 conversion, (2) CO_2 conversion, (3) H_2/CO ratio versus Mg molar fraction at various gas hourly space velocities (GHSV) over M-10NiyMg(90−y)Al catalysts; reaction conversions: $CH_4/CO_2 = 1$, 750 °C, 1 atm.

even exceeding the equilibrium conversions in the temperature ranges (650–800 °C) studied [2], demonstrating excellent catalytic activity. The advantageous catalytic properties might derive from the large specific surface areas and big pore volumes of these mesoporous catalysts, which could provide more "accessible" Ni active sites for the gaseous reactants finally leading to better
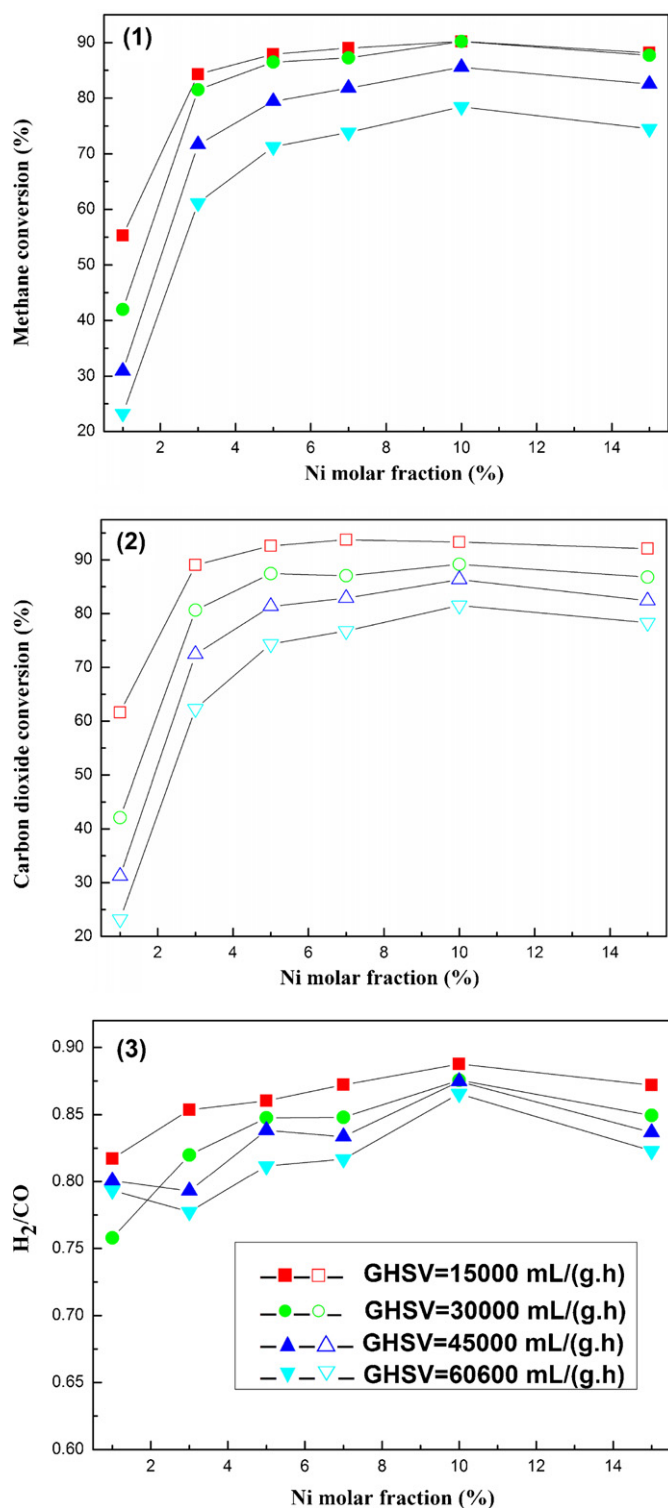
Fig. 13. The curves of the (1) CH_4 conversion, (2) CO_2 conversion, (3) H_2/CO ratio versus Ni molar fraction at various gas hourly space velocities (GHSV) over M-xNi2Mg(98 − x)Al catalysts; reaction conversions: CH_4/CO_2 = 1, 750 °C, 1 atm.

catalytic activity. The promoting effect of the Mg modifier was not extremely obvious when the reaction was carried out in relative low gas flows (GHSV = 15,000 mL/(h g)). Overall, all the catalysts performed similar catalytic properties, suggesting that they could provide sufficient Ni active sites for the reactants.

The effects of Mg on the catalytic performances of M-10NixMg(90 − x)Al catalysts were illustrated in Fig. 12. The results

of CRM reaction at 750 °C over different catalysts expressed as the CH_4, CO_2 conversions versus Mg molar content were laid out in Fig. 12(1 and 2), respectively. On the whole, all the M-10NiyMg(90 − y)Al catalysts possessed fairly high catalytic conversions in CRM reaction even when the GHSV was up to 60,600 mL/(g h) (CH_4 > 70.0%, CO_2 > 73.0%) thanks to the large specific surface areas and big pore volumes (see Table 1) of these materials, which could provide more "accessible" Ni actives for the reactants. Whereas, with the increase of the GHSV from 15,000 to 60,600 mL/(g h), the conversions of CH_4 and CO_2 also suffered from big decline. The reason for this might derive from the reduction in the residence time of the reactants on the surface of the catalysts. As a result, the thermodynamic equilibrium could not be achieved due to insufficient contact time, leading to the decrease of the catalytic activity. Besides, it could be observed that the curves in these two figures were still identical in the shapes even when the GHSV changed, indicating that the effects of Mg on the conversions of CH_4 and CO_2 followed the analogical rules. As shown in the figures, the CH_4 and CO_2 conversions mounted up as the Mg content increased in the initial stage and achieved the maximum when the content of Mg reached 2%. However, excessive addition of Mg acted oppositely. With the further addition of Mg up to 10%, the conversions decreased monotonically. It was necessary to explain these unique phenomena appearing over these catalysts caused by the addition of Mg.

Obviously, these curves were similar to the "volcano-shaped curve" in the shape, which was fairly popular in the field of catalysis. It was generally believed that the Mg promoter increased the numbers of the basic sites on the surface of the catalysts and strengthened the chemisorption of the CO_2, which had been confirmed by the CO_2-TPD analysis (refer to Fig. 11). Besides, the doped Mg was beneficial to improve the dispersion of the nickel active sites. When the dosage of Mg was moderate, the chemisorption and activation of the CO_2 were simultaneously promoted. Hence, the CO_2 concentration on the surfaces of the catalysts ought to be larger than that of feedstock gas stream, leading to higher CH_4, CO_2 conversions. Nevertheless, the excessive addition of Mg in turn restrained the further increase of the conversions of the reactants. Similar situations were also encountered in the pioneer literatures with K_2O, Cs_2O, CaO, BaO, etc. as promoters [45–48]. When the number of the basic sites was superfluous, the adsorbed CO_2 would cover the Ni active sites of the catalysts and desorption from the active sites became difficult due to the strong alkaline sites among the frameworks of the catalysts. Consequently, the subsequent adsorption and activation of the carbon dioxide were blocked, finally leading to the decline of the CH_4, CO_2 conversions. At the same time, the previous work also found higher amount of alkaline centers would cover some amount of the Ni, block the accessibility of the methane, and then decrease the reforming activity [47]. As we all knew, the catalytic behavior of the catalyst was the synergy of size, structure, composition, and so on [22]. Therefore, the improved the catalytic activity could be obtained only when the dosage of Lewis base promoter (MgO) was moderate.

The relationship between the H_2/CO ratio and the Mg loading as well as GHSV for the CRM reaction was also investigated in Fig. 12(3). It was found that the H_2/CO ratio almost did not vary with alteration in the Mg loading as well as the GHSV. As observed in the figure, the H_2/CO ratio always fluctuated around 0.85 regardless of the changes in Mg dosage and GHSV while the reaction was implemented at 750 °C. On the contrary, the H_2/CO ratio was more inclined to be related with the reaction temperature (see Table 3). The reason for this was that the RWGS reaction was greatly sensitive to the reaction temperatures and ultimately influenced the variation of the H_2/CO ratio.
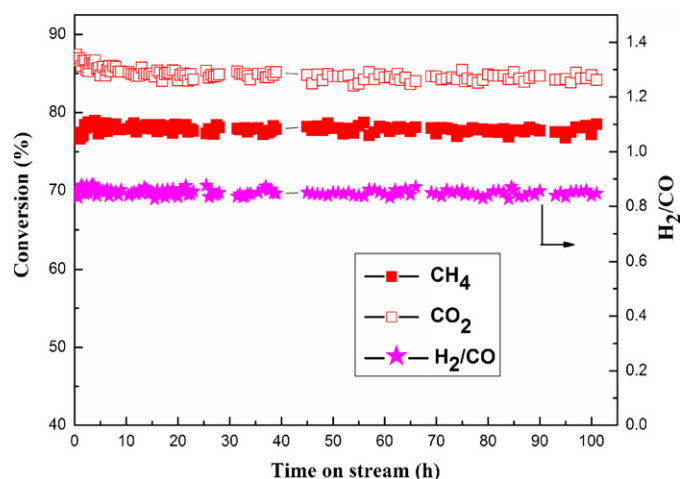
Fig. 14. Long-term stability test over the M-15Ni2Mg83Al catalyst; reaction conditions: $CH_4/CO_2 = 1$, GHSV = 15,000 mL/(g h), 700 °C, 1 atm.

Fig. 16. TPH profile of the 100 h endurance-tested M-15Ni2Mg83Al catalyst.

3.7.2. The effect of the Ni content

The effect of the Ni molar content on the catalytic activity for the M-xNi2Mg(98 − x)Al catalysts was also detailedly studied. The dependence of the initial catalytic activity on the Ni molar content at various temperatures under given conditions ($CH_4/CO_2 = 1$, GHSV = 15,000 mL/(g h), 1 atm) was summarized in Table 4. It was found that the conversions of CH_4, CO_2 originally increased with increasing the Ni loading from 1% to 10% and suffered from a little decline with the further increase of Ni content up to 15% in all temperature ranges studied. Took the catalytic behaviors at 650 °C as an example. As the Ni loading increased from 1% to 15%, the conversions of the CH_4, CO_2 initially experienced rapid augment from 23.57%, 25.84% for 1% Ni content to 59.52%, 65.96% for 5% Ni loading, respectively. Subsequently, the growth rates for them were slowed down and ultimately reached the summit at 10% (66.08%, 71.45% for CH_4, CO_2 conversions, respectively). Further increase in Ni loading acted oppositely. Compared with 10% sample, CH_4, CO_2 conversions underwent a slight decline for 15%. CH_4 and CO_2 conversions had been close to or even exceeding their equilibrium conversions when the Ni loading was greater than or equal to 5%. The catalytic performances at other temperature stages also possessed parallel tendency. This indicated that the M-xNi2Mg(98 − x)Al catalysts could provide sufficient Ni active sites for the reactants to reach thermodynamic equilibrium conversion when the Ni loading was
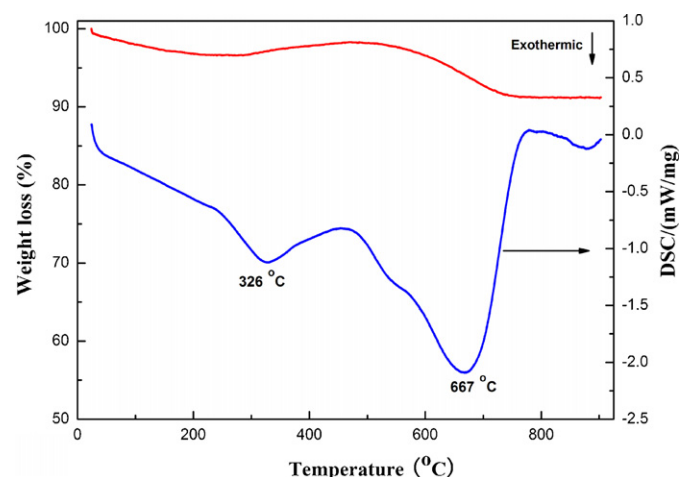

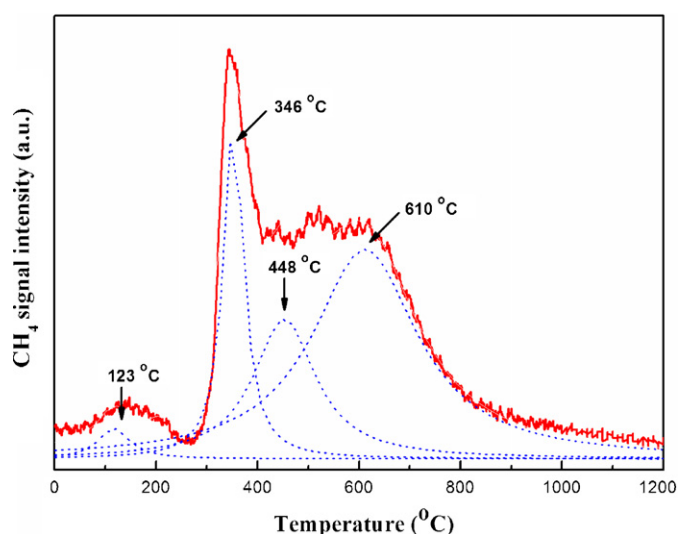**Fig. 15.** TG–DSC analysis of the 100 h endurance-tested M-15Ni2Mg83Al catalyst.

as low as 5%. The outstanding catalytic properties for these mesoporous catalysts might also originate their large specific surface areas and big pore volumes, which enabled the reactants to expose to more Ni active sites at a low Ni loading.

As for the H_2/CO ratio, similar to the data in Table 3, the H_2/CO ratio was also less than 1/1 and increased as the temperature elevated due to the presence of the RWGS. Besides, it seemed to be closely related with the Ni content when the reaction temperature kept constant. On the whole, as the Ni content increased, the H_2/CO ratio was inclined to hoist. The reason for this might be derived from the inhibitory effect of Ni based catalysts towards the RWGS reaction. In addition to these, all the catalysts also behaved their highest catalytic activities at 800 °C in the temperature scope studied, once again reflecting the intense endothermic character of the dry reforming.

Besides, catalytic behaviors of various GHSV from 15,000 to 60,600 mL/(g h) for M-xNi2Mg(98 − x)Al were also investigated. As shown in Fig. 13(1 and 2), the slopes of the curves were very steep when the Ni containing initially increased from 1% to 3%, then became smaller, and finally reached the summit at 10 M% fraction of Ni. Further increase in the Ni content, the CH_4, CO_2 conversions suffered a little decline. When the GHSV was kept at 15,000 mL/(g h), the original augment of the Ni content from 1% to 5% in M-xNi2Mg(98 − x)Al catalysts could provide the reactants with more active sites, leading to the sudden increase in the CH_4, CO_2 conversions. Then their conversions reached a platform due to their sufficient active sites for the feed stock gases. Whereas, as the GHSV increased, the advantage of M-10Ni2Mg88Al catalyst became more and more remarkable. The reason for the outstanding performances for M-10Ni2Mg88Al compared to other M-xNi2Mg(98 − x)Al catalysts might derive from its more adequate active centers. Compared with other M-xNi2Mg(98 − x)Al with Ni molar content less than 7%, the M-10Ni2Mg88Al was originally able to provide more active sites than those catalysts. As for the M-15Ni2Mg83Al sample, a bit sintering of the metallic active sites might took place after going through the severe reduction and reaction stages. Furthermore, the connections between H_2/CO ratio and GHSV as well as Ni content were also studied in Fig. 13(3). Similar to the results presented in Table 4, the H_2/CO tended to increase as the Ni containing augment due to the inhibitory effect of the Ni on the RWGS. As the GHSV increased, the H_2/CO also suffered some decrease for most catalysts. However, their interaction mechanism was not quite clear and required further study.

Table 4
The average conversions of the CH_4, CO_2 and H_2/CO ratios for the CRM reaction over M-xNi2Mg(98 − x)Al catalysts at various temperatures; reaction conditions: $CH_4/CO_2 = 1$, GHSV = 15,000 mL/(g h), 1 atm.

Samples	650 °C			700 °C			750 °C			800 °C		
	C_{CH_4}	C_{CO_2}	H_2/CO	C_{CH_4}	C_{CO_2}	H_2/CO	C_{CH_4}	C_{CO_2}	H_2/CO	C_{CH_4}	C_{CO_2}	H_2/CO
M-15Ni2Mg83Al	62.50	68.60	0.8065	78.12	83.07	0.8415	88.19	92.10	0.8721	94.64	95.90	0.8908
M-10Ni2Mg88Al	66.08	71.45	0.8448	80.94	85.69	0.8601	90.22	93.32	0.8876	95.08	96.25	0.8859
M-7Ni2Mg91Al	59.14	66.88	0.7963	78.40	83.46	0.8375	89.00	93.74	0.8722	94.82	96.53	0.9032
M-5Ni2Mg93Al	59.52	65.96	0.8064	76.64	82.37	0.8495	87.93	92.62	0.8604	94.86	96.30	0.8926
M-3Ni2Mg95Al	40.23	44.40	0.7863	63.84	69.28	0.8181	84.31	89.07	0.8536	93.00	95.79	0.8857
M-1Ni2Mg97Al	23.57	25.84	0.6989	36.50	40.45	0.7755	55.31	61.60	0.8173	69.46	75.30	0.8641

3.7.3. Catalytic behaviors of M-xNiyMgzAl catalysts in long-term stability test

Exploring stable catalysts was the major issue in CRM reaction. The evaluation of the long-term stability of the catalyst was performed under given conditions: $CH_4/CO = 1$, 700 °C, GHSV = 15,000 mL/(g h), 1 atm. The M-15Ni2Mg88Al material was chosen as the catalyst for the long lifetime test, because it was more prone to suffer from the sintering of the Ni active centers during the reduction and reaction stages due to its relatively higher Ni content than that of other samples. As shown in Fig. 14, M-15Ni2Mg88Al catalyst exhibited high catalytic activity (around 78%, 83% for the conversions of CH_4, CO_2, respectively) and rather stable catalytic behavior in the whole 100 h time on stream. As mentioned above, the excellent catalytic activity should be attributed to the merits of the mesoporous structure, which would accommodate the reactants with much more "exposed" active centers due to its large specific surface area as well as pore volume. Besides, it was also well known that the reforming catalysts were generally subjected to several deactivation mechanisms including coking, sintering, and oxidation of the metallic phase, which would result in the decrease of the active metal sites on the catalyst surface and ultimately lower the catalytic stability [58,59]. Furthermore, it was also believed that smaller Ni particles had strengthened capability to suppress carbon deposition [2,3,24–27]. As for the M-15Ni2Mg83Al catalyst, the Ni active centers were inlayed in the mesoporous framework due to this unique one pot strategy. Therefore, the "confinement effect" of the mesopores limited the growth of the Ni particles during the reaction and promoted the catalytic stability due to the "size effect" of the Ni nanoparticles. In addition to this, the modified Mg improved the Lewis basicity of the material and was in favor of the chemisorption of CO_2, which would accelerate the procedure: $CO_2 + C = 2CO$ and then suppress the carbon deposition. Consequently, the excellent catalytic activity of M-15Ni2Mg83Al for long-term stability was preserved due to its high coke resistance ability.

3.8. TG–DSC analysis

The properties of the carbon deposition over M-15Ni2Mg83Al catalyst after 100 h long-term stability at 700 °C were shown in
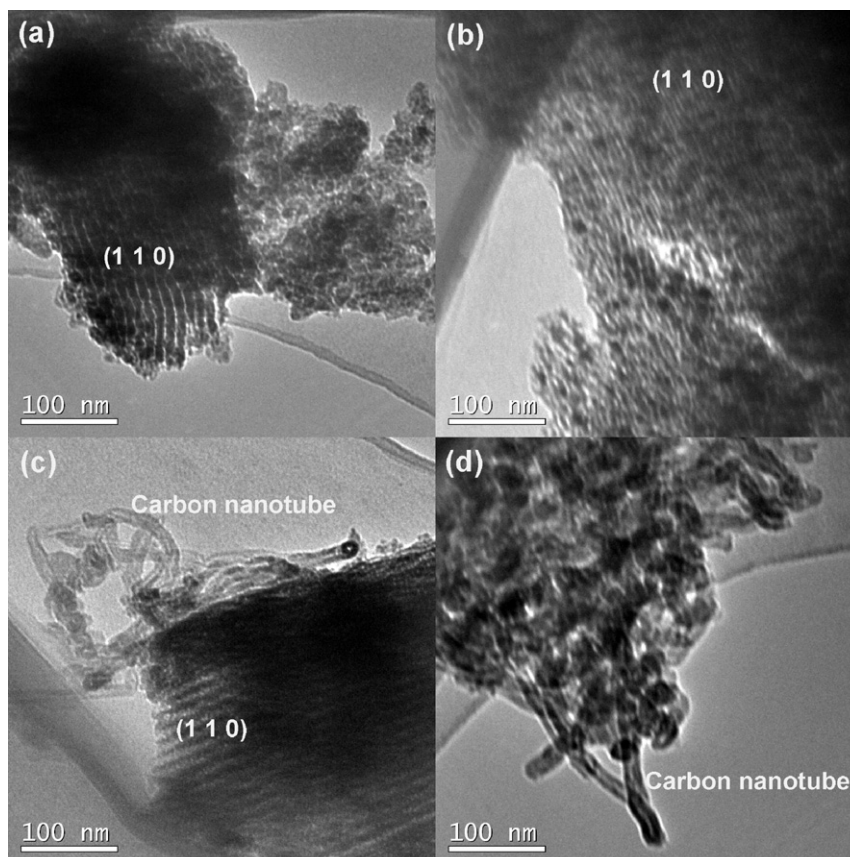

Fig. 17. TEM pictures of the 100 h endurance-tested M-15Ni2Mg83Al catalyst.

Fig. 15. As for TG curve, with the increase of the temperature, the general trend of the curves was downward. However, the curve initially experienced slight rise in the region from 250 °C to 400 °C, which might be derived from the oxidation of elemental Ni. The TG curve of the used catalyst indicated a weight loss due to the removal of the deposited carbon. The TG curve showed that the weight loss of the coke over the catalyst was only 7.0%. The DSC profile exhibited that the deposition carbon could be burned up in a temperature range between 240 and 780 °C. The two apparent exothermic peaks centered at 326 °C and 667 °C were also displayed in the DSC profile, implying that there were at least two sorts of carbon deposition on the Ni active sites. The exothermic peak around 326 °C was attributable to the combustion of the amorphous carbon, which was active species for the formation of synthesis gas [60,61]. Another peak at 667 °C was ascribed to the whisker type carbon (also known as carbon nanotube, refer to Fig. 17), which was responsible for the deactivation of the catalyst [62,63].

3.9. TPH of the endurance-tested catalyst

The TPH profile of the endurance-tested catalyst was also shown in Fig. 16. There were four peaks centered at 123 °C, 346 °C, 448 °C, 560 °C observed in the figure. The first small peak at very low temperature could be related to the extremely reactive carbonaceous species [64]. The second peak at about 346 °C might be the amorphous carbon on the nickel sites, which was related to $C\alpha$ according to the pioneer literatures [61,64–67]. The amorphous carbon ($C\alpha$) might be the reaction intermediate, which was responsible for the CO formation [60,61]. Besides, part of the $C\alpha$ could be converted into less active $C\beta$ through further dehydrogenation, polymerization, and re-arrangement of $C\alpha$ [22,30,68]. The third overlapped peak centered at 448 °C might be attributable to $C\beta$, which would be further gasified, and might encapsulate on the surface, or dissolve in or encapsulate the Ni crystallite. The last overlapped peak around 610 °C was identified as the whisker type carbon (carbon nanotube, see Fig. 17), which had the lowest reactivity compared with other deposition carbon species towards hydrogenation and contributed to the deactivation of the catalyst [69,70]. The characteristic result of the TPH was well consistent with the deduction based on the TG–DSC analysis.

3.10. Morphology analysis of the endurance-tested catalyst

In order to further confirm the morphology of the coke as well as the outstanding thermal stability of the material, TEM analysis of the 100 h endurance-tested M-15Ni2Mg83Al was performed. The images were displayed in Fig. 17. The uniform mesopores along [1 1 0] direction were clearly seen from Fig. 17(a–c), implying that the ordered mesostructure of M-15Ni2Mg83Al was successfully maintained. As shown in Fig. 17(c and d), the main coke residue over the spent catalyst observed was carbon nanotubes. Moreover, it was worthy noting that the carbon nanotubes were mainly distributed outside of the mesopores according to Fig. 17(c). Consequently, the deactivation of the catalyst deriving from the coverage of Ni active centers by the coke (mainly from carbon nanotubes) was effectively avoided to some degree, accounting for no deactivation after 100 h lifetime endurance test. It was of interest that no obvious amorphous carbon was found. The reason for this might be that the amorphous carbon was evenly distributed among the mesopores and could be eliminated in the subsequent process of CO production.

4. Conclusion

Ordered mesoporous NiO–MgO–Al$_2$O$_3$ composite oxides with various Ni and Mg contents were facilely prepared *via* one pot evaporation-induced self-assembly strategy. The obtained materials possessed large specific surface areas, big pore volumes, uniform pore sizes, and favorable thermal stability. The catalytic performances of the materials for CRM reaction were excellent, displaying high catalytic activity and long catalytic stability. The ordered mesoporous framework of the M-xNiyMg(100-x-y)Al catalysts played a significant role to endow these merits for these catalysts, which could provide more "accessible" Ni active centers for the reactants and stabilized Ni nanoparticles by the "confinement effect" during the reaction. The effect of the modified Mg on the catalytic performances was also examined. It was found that only moderate addition of the Mg modifier could effectively promote the catalytic properties of the catalysts. Strong metal–support interaction between Ni atom and the mesoporous framework had been formed for all the materials with diverse Ni and Mg containing. The M-15Ni2Mg83Al catalyst exhibited intensive capacity of anti-coking due to the nano-sized Ni particles, which contributed to suppressing coke due to the "size effect". Although certain amount of coke formed on the surface of M-15Ni2Mg83Al catalyst, the activity did not decrease after 100 h lifetime test, suggesting that proportion of the carbon deposition was active in the reforming reaction. Because of these favorable properties, ordered mesoporous NiO–MgO–Al$_2$O$_3$ composite oxides could be considered as promising catalysts for CRM reaction.

References

[1] A.T. Ashcroft, A.K. Cheetham, M.L.H. Green, P.D.F. Vernon, Nature 352 (1991) 225–226.
[2] M.C.J. Bradford, M.A. Vannice, Catal. Rev.: Sci. Eng. 41 (1999) 1–42.
[3] Y.H. Hu, E. Ruckenstein, Catal. Rev.: Sci. Eng. 44 (2002) 423–453.
[4] J.G. Zhang, H. Wang, A.K. Dalai, J. Catal. 249 (2007) 300–310.
[5] J.T. Richardson, S.A. Paripatyadar, Appl. Catal. 61 (1990) 293–309.
[6] M.-S. Fan, A.Z. Abdullah, S. Bhatia, Appl. Catal. B: Environ. 100 (2010) 365–377.
[7] K. Seshan, Appl. Catal. A: Gen. 98 (1993) N18.
[8] B.Q. Xu, W.M.H. Sachtler, J. Catal. 180 (1998) 194–206.
[9] J.R.H. Ross, A.N.J. van Keulen, M.E.S. Hegarty, K. Seshan, Catal. Today 30 (1996) 193–199.
[10] S.B. Wang, G.Q.M. Lu, G.J. Millar, Energy Fuels 10 (1996) 896–904.
[11] M. Levy, R. Levitan, E. Meirovitch, A. Segal, H. Rosin, R. Rubin, Solar Energy 48 (1992) 395–402.
[12] M. Levy, R. Rubin, H. Rosin, R. Levitan, Energy 17 (1992) 749–756.
[13] J.M. Wei, B.Q. Xu, J.L. Li, Z.X. Cheng, Q.M. Zhu, Appl. Catal. A: Gen. 196 (2000) L167–L172.
[14] A.M. Gadalla, B. Bower, Chem. Eng. Sci. 43 (1988) 3049–3062.
[15] J.B. Claridge, M.L.H. Green, S.C. Tsang, A.P.E. York, A.T. Ashcroft, P.D. Battle, Catal. Lett. 22 (1993) 299–305.
[16] M.C.J. Bradford, M.A. Vannice, J. Catal. 183 (1999) 69–75.
[17] M. Sigl, M.C.J. Bradford, H. Knozinger, M.A. Vannice, Top. Catal. 8 (1999) 211–222.
[18] S. Damyanova, B. Pawelec, K. Arishtirova, J.L.G. Fierro, C. Sener, T. Dogu, Appl. Catal. B: Environ. 92 (2009) 250–261.
[19] S. Damyanova, B. Pawelec, K. Arishtirova, M.V.M. Huerta, J.L.G. Fierro, Appl. Catal. B: Environ. 89 (2009) 149–159.
[20] J. Nakamura, K. Aikawa, K. Sato, T. Uchijima, Catal. Lett. 25 (1994) 265–270.
[21] M.P. Kohn, M.J. Castaldi, R.J. Farrauto, Appl. Catal. B: Environ. 94 (2010) 125–133.
[22] C.J. Liu, J.Y. Ye, J.J. Jiang, Y.X. Pan, ChemCatChem 3 (2011) 529–541.
[23] S. Corthals, J. Van Nederkassel, H. De Winne, J. Geboers, P. Jacobs, B. Sels, Appl. Catal. B: Environ. 105 (2011) 263–275.
[24] Y.H. Hu, E. Ruckenstein, Catal. Adv. 48 (48) (2004) 297–345.
[25] H.S. Roh, K.W. Jun, Catal. Surv. Asia 12 (2008) 239–252.
[26] G. Jones, J.G. Jakobsen, S.S. Shim, J. Kleis, M.P. Andersson, J. Rossmeisl, F. Abild-Pedersen, T. Bligaard, S. Helveg, B. Hinnemann, J.R. Rostrup-Nielsen, I. Chorkendorff, J. Sehested, J.K. Norskov, J. Catal. 259 (2008) 147–160.
[27] Y.H. Hu, Catal. Today 148 (2009) 206–211.
[28] X. Zhu, P. Huo, Y. Zhang, D. Cheng, C. Liu, Appl. Catal. B: Environ. 81 (2008) 132–140.
[29] H.W. Chen, C.Y. Wang, C.H. Yu, L.T. Tseng, P.H. Liao, Catal. Today 97 (2004) 173–180.

[30] D.L. Trimm, Catal. Today 49 (1999) 3–10.
[31] K. Bourikas, C. Kordulis, A. Lycourghiotis, Catal. Rev.: Sci. Eng. 48 (2006) 363–444.
[32] N. Laosiripojana, S. Assabumrungrat, Appl. Catal. B: Environ. 60 (2005) 107–116.
[33] A.J. van Dillen, R. Terorde, D.J. Lensveld, J.W. Geus, K.P. de Jong, J. Catal. 216 (2003) 257–264.
[34] E.K. Poels, J.G. Dekker, W.A. Vanleeuwen, Prep. Catal. V 63 (1991) 205–214.
[35] G.S. Gallego, J.G. Marin, C. Batiot-Dupeyrat, J. Barrault, F. Mondragon, Appl. Catal. A: Gen. 369 (2009) 97–103.
[36] G.S. Gallego, F. Mondragon, J. Barrault, J.M. Tatibouet, C. Batiot-Dupeyrat, Appl. Catal. A: Gen. 311 (2006) 164–171.
[37] Z.L. Xu, M. Zhen, Y.L. Bi, K.J. Zhen, Catal. Lett. 64 (2000) 157–161.
[38] Z.L. Xu, M. Zhen, Y.L. Bi, K.J. Zhen, Appl. Catal. A: Gen. 198 (2000) 267–273.
[39] J.J. Guo, H. Lou, H. Zhao, D.F. Chai, X.M. Zheng, Appl. Catal. A: Gen. 273 (2004) 75–82.
[40] Y.G. Chen, K. Tomishige, K. Fujimoto, Chem. Lett. (1997) 999–1000.
[41] Y.G. Chen, K. Tomishige, K. Fujimoto, Appl. Catal. A: Gen. 161 (1997) L11–L17.
[42] K. Tomishige, O. Yamazaki, Y.G. Chen, K. Yokoyama, X.H. Li, K. Fujimoto, Catal. Today 45 (1998) 35–39.
[43] Y.H. Wang, H.M. Liu, B.Q. Xu, J. Mol. Catal. A: Chem. 299 (2009) 44–52.
[44] O. Yamazaki, T. Nozaki, K. Omata, K. Fujimoto, Chem. Lett. (1992) 1953–1954.
[45] S.G. Liu, L.X. Guan, J.P. Li, N. Zhao, W. Wei, Y.H. Sun, Fuel 87 (2008) 2477–2481.
[46] Z.Y. Hou, T. Yashima, Appl. Catal. A: Gen. 261 (2004) 205–209.
[47] P. Chen, Z.Y. Hou, X.M. Zheng, Chin. J. Chem. 23 (2005) 847–851.
[48] M. Rezaei, S.M. Alavi, S. Sahebdelfar, Z.F. Yan, Energy Fuels 22 (2008) 2195–2202.
[49] J.A.C. Dias, J.M. Assaf, Catal. Today 85 (2003) 59–68.
[50] T. Osaki, T. Mori, J. Catal. 204 (2001) 89–97.
[51] S.M. Morris, P.F. Fulvio, M. Jaroniec, J. Am. Chem. Soc. 130 (2008) 15210–15216.
[52] W.H. Shen, K. Komatsubara, T. Hagiyama, A. Yoshida, S. Naito, Chem. Commun. (2009) 6490–6492.
[53] Q. Yuan, A.X. Yin, C. Luo, L.D. Sun, Y.W. Zhang, W.T. Duan, H.C. Liu, C.H. Yan, J. Am. Chem. Soc. 130 (2008) 3465–3472.
[54] J.S. Beck, J.C. Vartuli, W.J. Roth, M.E. Leonowicz, C.T. Kresge, K.D. Schmitt, C.T.W. Chu, D.H. Olson, E.W. Sheppard, S.B. McCullen, J.B. Higgins, J.L. Schlenker, J. Am. Chem. Soc. 114 (1992) 10834–10843.
[55] C.T. Kresge, M.E. Leonowicz, W.J. Roth, J.C. Vartuli, J.S. Beck, Nature 359 (1992) 710–712.
[56] Y.L. Chu, S.B. Li, J.Z. Lin, J.F. Gu, Y.L. Yang, Appl. Catal. A: Gen. 134 (1996) 67–80.
[57] L. Pino, A. Vita, F. Cipiti, M. Lagana, V. Recupero, Appl. Catal. B: Environ. 104 (2011) 64–73.
[58] J. Sehested, J. Catal. 217 (2003) 417–426.
[59] X. Hu, G.X. Lu, Appl. Catal. B: Environ. 99 (2010) 289–297.
[60] Y.G. Chen, J. Ren, Catal. Lett. 29 (1994) 39–48.
[61] H.M. Swaan, V.C.H. Kroll, G.A. Martin, C. Mirodatos, Catal. Today 21 (1994) 571–578.
[62] S.B. Wang, G.Q. Lu, Energy Fuels 12 (1998) 248–256.
[63] H.T. Liu, S.Q. Li, S.B. Zhang, L. Chen, G.J. Zhou, J.M. Wang, X.L. Wang, Catal. Lett. 120 (2008) 111–115.
[64] M. Rezaei, S.M. Alavi, S. Sahebdelfar, Z.F. Yan, J. Nat. Gas Chem. 17 (2008) 278–282.
[65] C.H. Bartholomew, Catal. Rev.: Sci. Eng. 24 (1982) 67–112.
[66] C. Mirodatos, H. Praliaud, M. Primet, J. Catal. 107 (1987) 275–287.
[67] M. Rezaei, S.M. Alavi, S. Sahebdelfar, P. Bai, X.M. Liu, Z.F. Yan, Appl. Catal. B: Environ. 77 (2008) 346–354.
[68] D.L. Trimm, Catal. Today 37 (1997) 233–238.
[69] Z.L. Zhang, X.E. Verykios, Catal. Today 21 (1994) 589–595.
[70] J. Guo, H. Lou, X.M. Zheng, Carbon 45 (2007) 1314–1321.